Electronic Supplementary Material (ESI) for Nanoscale.

Supporting Information

Magnetic micromotors crossing lipid membranes

Miguel A. Ramos Docampo,[a] Ondrej Hovorka,[b] Brigitte Städler[*a]*

[a]Interdisciplinary Nanoscience Center (iNANO), Aarhus University, Gustav Wieds Vej 14, 8000 Aarhus, Denmark.

[b]Faculty of Engineering and Physical Sciences, University of Southampton, SO16 7QF, Southampton, U.K.

*bstadler@inano.au.dk

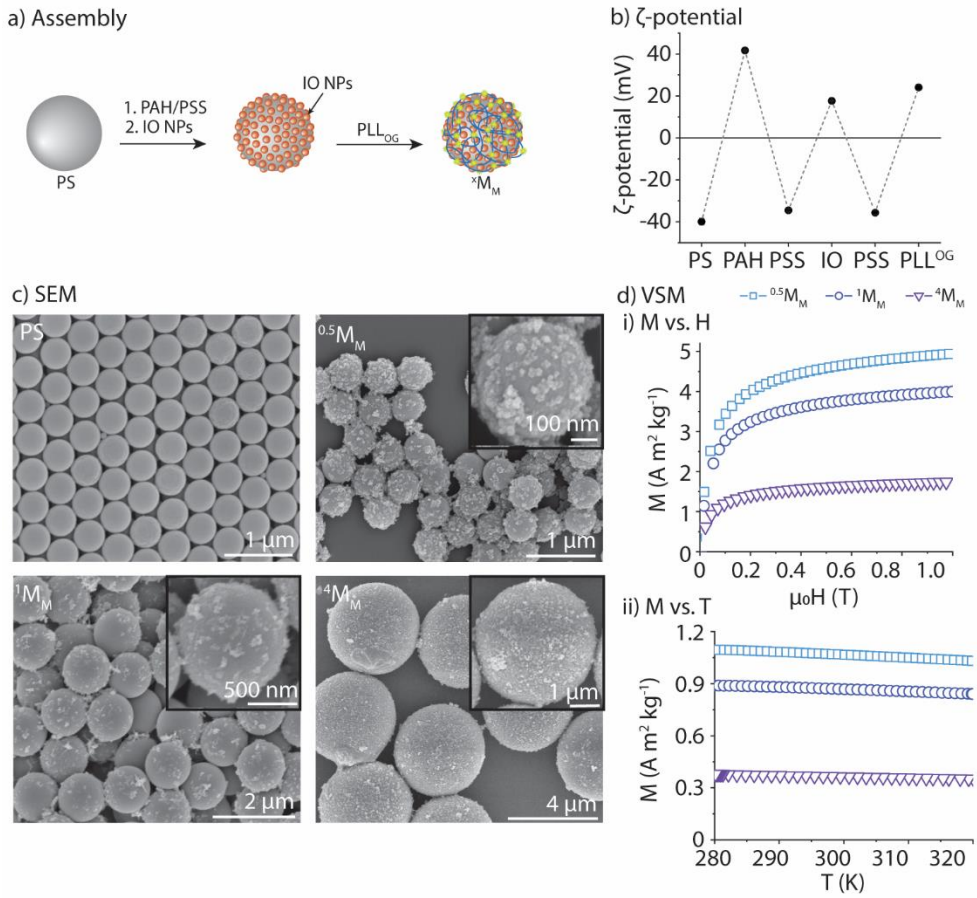

Figure S1. Magnetic motor ($^{x}M_{M}$) assembly. a) Polystyrene (PS) particles were coated with iron oxide nanoparticles (in orange) via the layer-by-layer technique, to yield in $^{x}M_{M}$. b) ζ-potential measurement of the subsequent materials deposited via layer-by-layer for $^{0.5}M_{M}$. c) Representative SEM images of the bare polystyrene (PS) particles, and the motors upon deposition of the iron oxide (IO) nanoparticles. Insets are zoomed images of the motors. d) The magnetic behavior of the four assemblies was evaluated by vibrating sample magnetometry (VSM). The magnetization (M) vs. field (H) curves were recorded at 300 K (i) and magnetization vs. temperature curves were recorded at low field (100 mT) (ii).

Magnetic Motor Assembly. Magnetic motors are convenient candidates for self-propelling nanoparticles due to the easy controlled locomotion via the use of harmless magnetic fields.[1] We chose the simplest magnetic motor that could be easily driven by an external magnetic field, as the goal is to identify the interactions with lipid membranes and not the design of a novel class of motor. Magnetic motors of different sizes ($^{x}M_{M}$, *x* represents the core diameter in microns) were assembled using the layer-by-layer technique (Figure S1a). 0.5, 1 and 4 µm polystyrene (PS) particles were coated with a bilayer of poly(allylamine hydrochloride)/poly(sodium 4-styrenesulfonate) (PAH/PSS) followed by the deposition of iron oxide nanoparticles that were capped with PSS/poly(L-lysine) (PLL), yielding in $^{0.5}M_{M}$, $^{1}M_{M}$ and $^{4}M_{M}$. For visualization purposes, the motors were coated with an terminating layer containing

Oregon Green 488-modified poly(L-lysine) (PLL_{OG}) instead of PLL. The iron oxide particles with an average diameter of ~10 nm and a positive surface charge were synthesized using the Massart's method as previously reported.[2,3] The succcessful assembly was monitored by ζ-potential measurements using the 0.5 µm PS particles as representanive examples (Figure S1b). Scanning electron microscopy (SEM) images confirmed comparable iron oxide nanoparticles coating densisties for the different sized motors (Figure S1c). The magnetic response of the three types of motors was determined in a Physical Property Measurement System operating in vibrating sample magnetometry (VSM) mode. $^{0.5}M_M$ showed a saturation magnetization of 4.9 A m^2 kg^{-1} at 1 T, which decrased to 4.0 and 1.7 m^2 kg^{-1} for $^{1}M_M$ and $^{4}M_M$, respectively (Figure S1di). These results allowed to estimate the mass percertage of magnetic material present in each sample, which was ca. 68%, 40% and 17% for $^{0.5}M_M$, $^{1}M_M$ and $^{4}M_M$, respectively. The magnetization-temperaure curves were used to calculate the (volummetric) magnetic susceptibility (χ) in the range of temperatures where the experiments were conducted (Figure S1dii). As expected, χ decreased with the motor size, i.e., with increasing mass of non-magnetic (paramagnetic) material (PS). These values were found to be 2.4, 1.4 and 0.4 for $^{0.5}M_M$, $^{1}M_M$ and $^{4}M_M$, respectively.

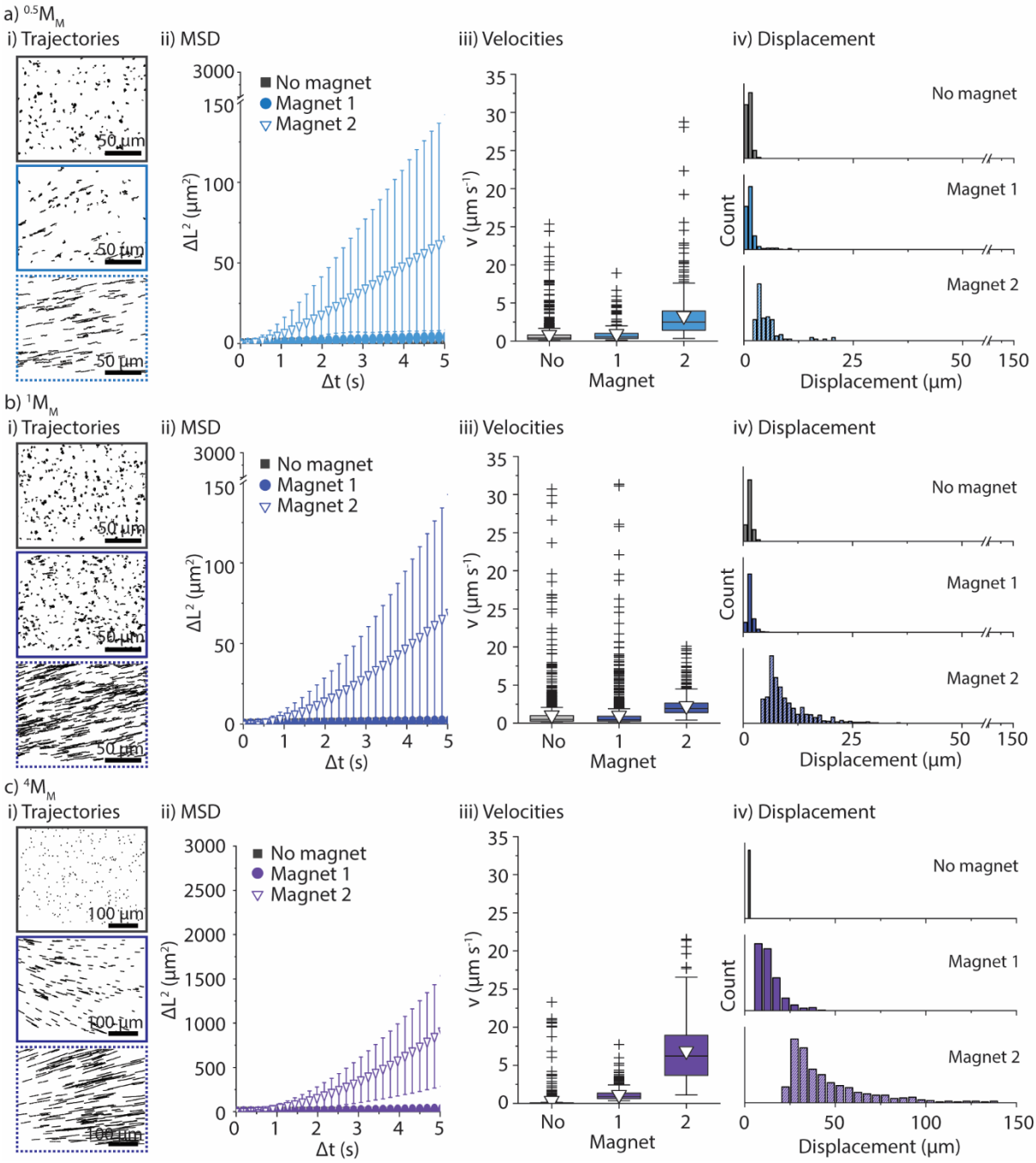

Figure S2. Locomotion of a) $^{0.5}M_M$, b) $^{1}M_M$, and c) $^{4}M_M$ in isotonic solution. For each type of motor, the representative trajectories in the absence (grey) or presence of magnet 2 (light blue, dark blue and purple, solid lines) or magnet 1 (light blue, dark blue and purple, dashed lines) are shown (i) as well as the average MSD (ii), the velocities presented as whisker plots (iii) and the displacement (iv) of the motors. MSD data are shown as average ± standard deviation (n = 2).

Locomotion in Isotonic Solution. The mobility of the motors was assessed in an isotonic solution (i.e., a solution containing 5 wt.% glucose and 0.9 wt.% NaCl) when exposed to a magnetic field in a microfluidic channel. The

magnetic field was created using a magnet with a pulling force of either 0.3 N or 2 N, which produced a magnetic flux gradient the motors would be pulled towards. (Note: the magnetic force refers to the force the magnet has to hold a magnetic object, given the provider specifications. The specific magnetic force of the 2 N is ~8× higher than the 0.3 N magnet. For simplicity, the notation magnet 1 and magnet 2 referring to the 0.3 N and the 2 N magnet, respectively, will be used in this article).

The trajectories of $^{0.5}M_M$ were analyzed in the presence of the magnetic field and compared to the Brownian motion of $^{0.5}M_M$ (Figure S2ai and Movie panel S1). As expected, the trajectories of $^{0.5}M_M$ became directional when the magnetic field was applied. Furthermore, the use of magnet 2, as opposed to magnet 1, resulted in an increase in the length of these trajectories. This observation was supported by the mean-squared displacement (MSD) plots (Figure S2aii), which changed from linear to parabolic when the magnetic field was applied. The analysis of the mobile and non-mobile $^{0.5}M_M$ in an ensemble was carried out and represented as whisker plots (Figure S2aiii). The $^{0.5}M_M$ showed an increased velocity from ~0.5 to ~3 µm s^{-1} when magnet 2 was used. The median (line crossing the box) was below the average (triangle), which indicated a tendency towards slower speeds for most of the $^{0.5}M_M$ in the ensemble. However, there was also a fraction of very fast motors (represented as outliers) that reached ~30 µm s^{-1}, likely due to the inhomogeneous coating or the formation of chain-like aggregates during the locomotion. The displacement of $^{0.5}M_M$ was analyzed and represented as histograms (Figure S2aiv). Displacements of up to 5 µm were found for the Brownian motion of $^{0.5}M_M$, which increased up to 15 µm (magnet 1) and 40 µm (magnet 2) when the magnets were applied, confirming the expected locomotion characteristics.

A similar behavior was found for $^{1}M_M$ and $^{4}M_M$. The trajectories changed from Brownian to directed motion when the magnetic fields were used (Figure S2bi/ci and Movie panels S2/S3). The MSD plots strongly agreed with the trajectories (Figure S2bii/cii), changing from linear to parabolic in all cases. The maximum velocities were ~3 µm s^{-1} for $^{1}M_M$ and ~7 µm s^{-1} for $^{4}M_M$ when magnet 2 was used (Figure S2biii/ciii). This increase in velocity with size was expected as more magnetic material was deposited and agreed with the magnetophoretic mobility coefficient (vide infra). As for $^{0.5}M_M$, all samples showed a trend to slower motors with a fraction of small very fast motors. As expected, longer displacements were always found when magnet 2 was employed, reaching up to ~40 µm and ~130 µm for $^{1}M_M$ and $^{4}M_M$, respectively (Figure S2biv/civ).

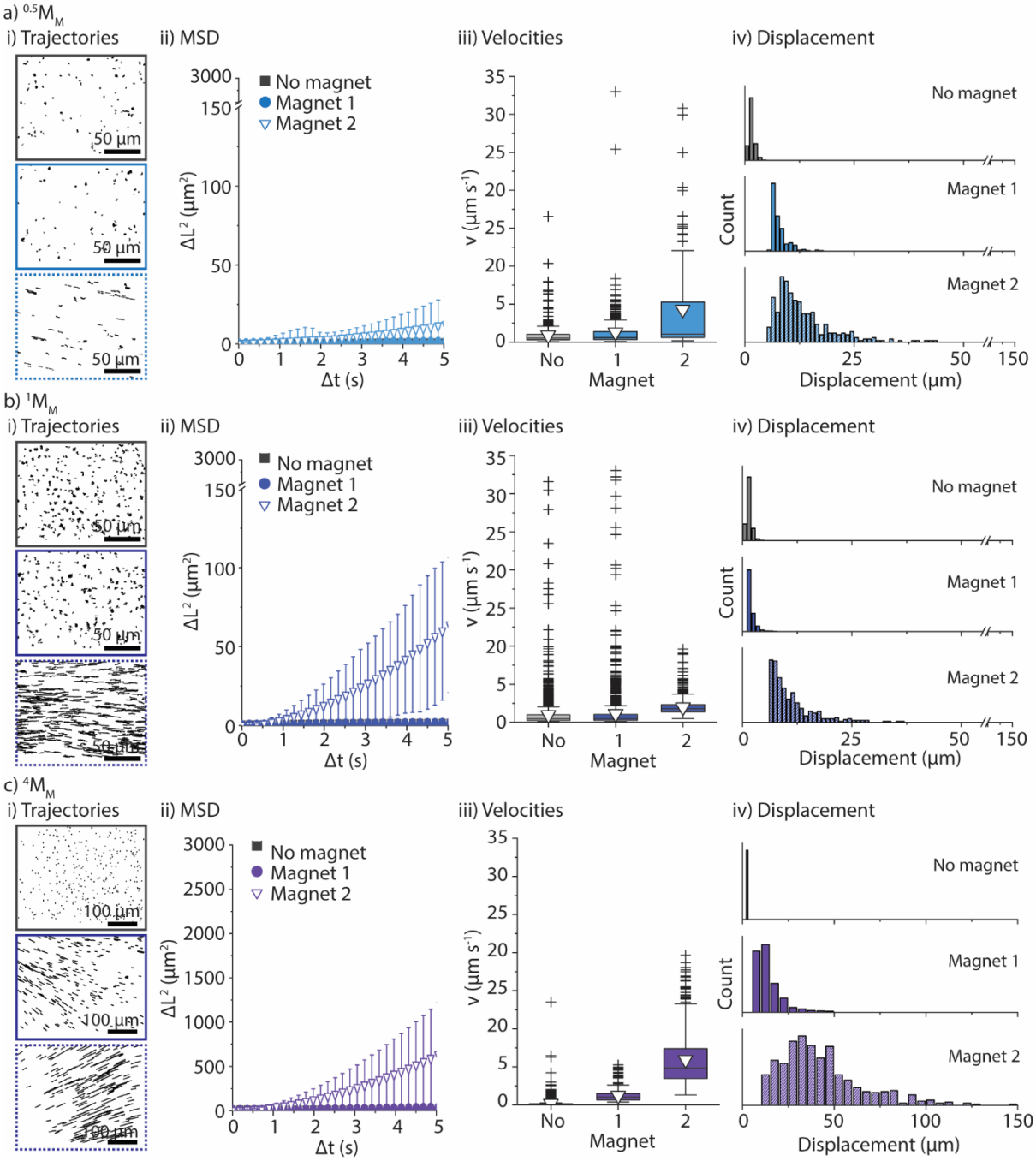

Figure S3. Locomotion performance of a) $^{0.5}M_M$, b) $^{1}M_M$, and c) $^{4}M_M$ in sucrose solution. For each motor, the representative trajectories in the absence (grey) or presence (light blue, dark blue and purple) of the magnetic field are shown (i). Averaged MSD (ii), velocities presented as whisker plots (iii), and the displacement (iv) of the motors are shown. Data are shown as average ± standard deviation (n = 2).

Locomotion in Sucrose Solution. Alternatively, the locomotion of $^{0.5}M_M$, $^{1}M_M$, and $^{4}M_M$ was assessed in sucrose solution (Figure S3 and Movie panels S1/S2/S3). In general, the trend was the same as in the isotonic solution, i.e., motors showed random trajectories that became ballistic when the magnetic field was applied. However, all tested

motors showed an overall lower average velocity, shorter displacement, and higher variability within the samples, due to the higher viscosity of the medium that affected the motors' mobility. (Please, note that the sucrose solution had a viscosity ~2× higher than the isotonic solution).

Following on, the magnetophoretic mobility coefficient (ξ) of the motors was estimated in both, the isotonic solution and in sucrose (Table S1). This parameter accounts for the mobility of magnetic particles in solution when a magnetic force is applied. The results indicated an increase in ξ with increasing motor size, i.e., ξ = 1.4 $\times 10^{-23}$, 2.5 $\times 10^{-23}$ and 14.1 $\times 10^{-23}$ $m^3\ T^{-1}\ A^{-1}\ s^{-1}$ for $^{0.5}M_M$, $^{1}M_M$ and $^{4}M_M$ in isotonic solution, respectively. In sucrose solution, the values were found to be ~2× lower, which was expected since the solution viscosity was higher. These results might explain the longer trajectories observed for $^{4}M_M$, which despite having the lowest magnetization, showed a stronger response to the magnetic field. We would like to note that these values are an estimation, and other experimental factors are likely to affect the actual performance of the motors (e.g., interactions between the motors and the environment or cooperative effects between the motors).

Table S1. Magnetophoretic mobility (ξ) values of $^{0.5}M_M$, $^{1}M_M$, and $^{4}M_M$ calculated from eq. 1, considering the viscosity (η) of the two solutions at 25 °C. R_p and R_H stand for solid particle and hydrodynamic radii, respectively. Δχ is the volumetric magnetic susceptibility.

Motor	Medium	η (mPa·s)	R_p (μm)	R_H (μm)	Δχ	ξ $\times 10^{-23}$ (m^3/T·A·s)
$^{0.5}M_M$	Isotonic solution	1.01	0.25	0.3	2.39	1.37
	Sucrose solution	2.17	0.25	0.3	2.39	0.64
$^{1}M_M$	Isotonic solution	1.01	0.5	0.75	1.36	2.49
	Sucrose solution	2.17	0.5	0.75	1.36	1.16
$^{4}M_M$	Isotonic solution	1.01	2.0	2.4	0.39	14.1
	Sucrose solution	2.17	2.0	2.4	0.39	6.59

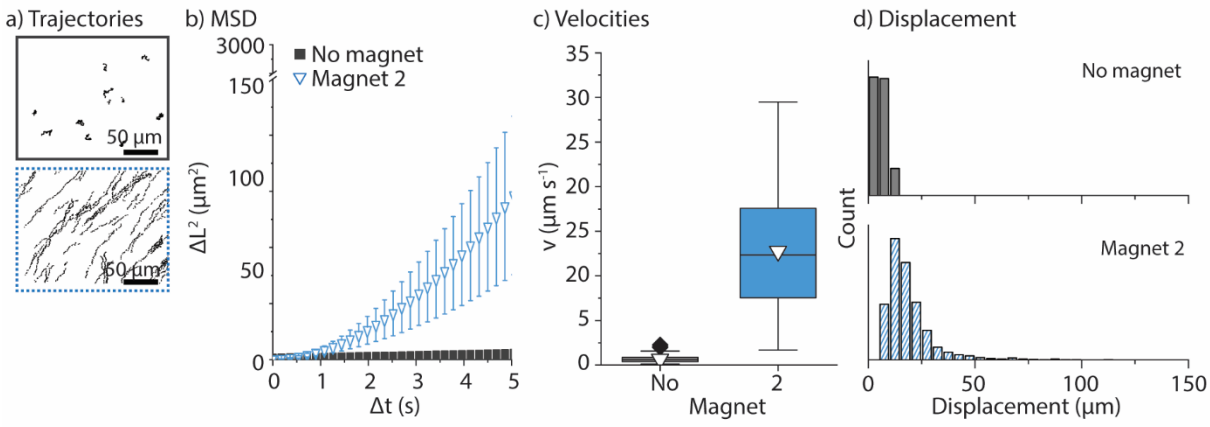

Figure S4. Locomotion performance of $^{0.5}M_{M\text{-}PEG}$ in isotonic solution. For each motor, the a) representative trajectories in the absence (grey) or presence (blue) of the magnetic field are shown. b) Averaged MSD, c) velocities presented as whisker plots, d) and the displacement of the $^{0.5}M_{M\text{-}PEG}$ are shown. Data are shown as average ± standard deviation (n = 2).

Non-interacting motors. Further, to assemble motors with an inert surface, poly(L-lysine)-grafted-poly(ethylene glycol) (PLL-*g*-PEG) was used as the terminating layer instead of PLL to obtain $^{0.5}M_{M\text{-}PEG}$. The locomotion was assessed in isotonic solution using magnet 2. $^{0.5}M_{M\text{-}PEG}$ showed longer trajectories (Figure S4 and Movie panel S4) when the magnetic field was applied, which was also reflected in the parabolic MSD curve. The maximum velocity of $^{0.5}M_{M\text{-}PEG}$ was ~22 µm s^{-1}, which was ~7× higher than for $^{0.5}M_M$. This observation was reported before for PEGylated motors,[2] and explained by the reduced interactions with the microfluidic channel surface due to the PEG coating. The displacement was ~2× larger, reaching up to ~50 µm when the magnet was employed.

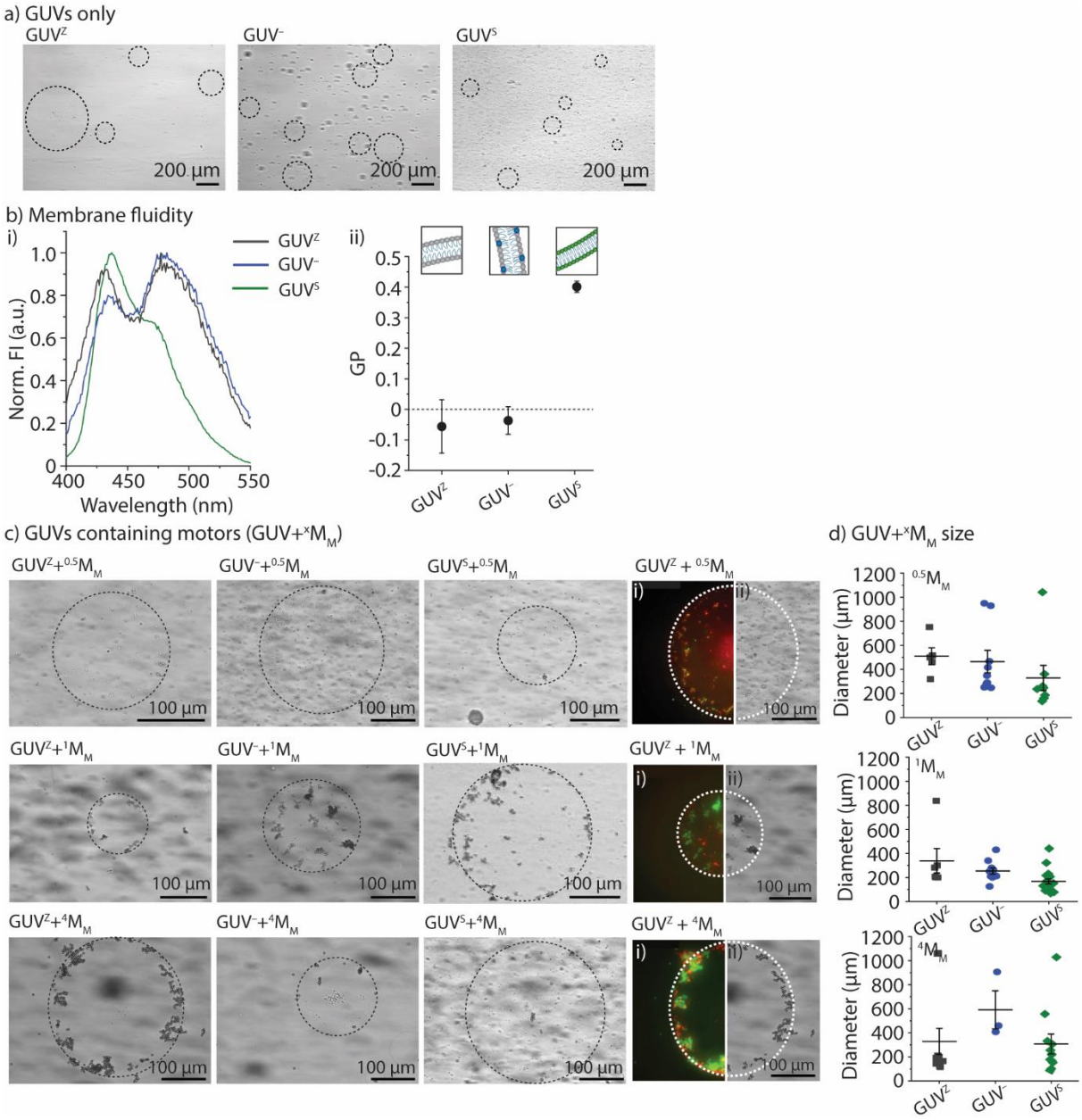

Figure S5. Giant unilamellar vesicles (GUVs) assembly. a) Representative bright-field microscopy images of GUV^Z, GUV$^-$ and GUV^S only. b) Normalized fluorescence emission spectra of GUV^Z, GUV$^-$ and GUV^S upon interaction with the Laurdan probe (i). The membrane fluidity was assessed by estimating the general polarization (GP) of the different GUV membranes using the fluorescent probe Laurdan (ii). Data are shown as average ± standard deviation (n = 2). c) Representative bright-field microscopy images of GUV^Z, GUV$^-$, GUV^C and GUV^S (rows from the top) containing $^{0.5}M_M$, ^1M_M, and ^4M_M (columns from left to right). The last column shows representative epifluorescence (i) and bright-field (ii) microscopy images of GUV^Z encapsulating $^{0.5}M_M$, ^1M_M and ^4M_M. The dotted circles are used to guide the eye and indicate the GUV membrane. (Green: PLL$_{OG}$, red: Rho-PE). d) Size distribution of GUV containing motors represented as whisker plots (n = 3 – 5).

Assembly of giant unilamellar vesicles (GUVs). Giant unilamellar vesicles (GUVs) are typically large (in the micrometer scale) spherical lipid-based structures that are used as simple model of the plasma membrane.[4] They offer therefore a good model to assess the interaction of motors and lipid membranes. GUVs were obtained by an emulsion-transfer method[5–7] (Figure S5a). Compared to other strategies,[8] this approach is more suitable for the encapsulation of cargo in the aqueous void of the GUVs. However, the membrane stability can be compromised (e.g., due to oil integrated in the membrane), and the yield can be lower than for other methods (e.g., electroformation). A 300 mM sucrose solution was employed to have the same osmotic pressure inside and outside of the GUVs. GUVs with varied lipid compositions were assembled in order to have a detailed overview of how the different GUVs' surface charge and membrane fluidity affected their interaction with the magnetic motors. Pristine 1,2-dioleoyl-*sn*-glycero-3-phosphocholine (DOPC) lipids were employed to make highly fluid, zwitterionic GUVs (GUV^{Z}). Negatively charged GUVs were obtained by mixing 10 wt. % 1,2-dioleoyl-*sn*-glycero-3-phospho-L-serine (DOPS) lipids with the DOPC lipids, yielding GUV^{-}. Finally, the fluidity of the membrane was decreased using saturated 1,2-dipalmitoyl-*sn*-glycero-3-phosphocholine (DPPC) lipids resulting in GUV^{S}. For visualization purposes, 0.5 wt. % 1,2-dipalmitoyl-*sn*-glycero-3-phosphoethanolamine-N-(lissamine rhodamine B sulfonyl) (ammonium salt) (Rho-PE) was added to the assemblies. (For details on GUV composition, please refer to Table S2). There were limited variations observed in terms of size and yield of the assemblies depending on the lipid composition. The size ranged from 200 – 600 µm and the yield was small. We also noted that the stability of the GUV was low, and some of them burst upon addition into the microfluidic channel for visualization. Hence, all experiments were conducted within 24 h after fabrication. A minimum of 10 independent GUVs from different assemblies were visualized per experiment to obtain conclusive results. We expected a change in the membrane fluidity due to the incorporation of different types of lipids. Therefore, the membrane fluidity of the three types of GUVs was determined by the fluorescent probe Laurdan.[9,10] Laurdan is a small organic molecule with an emission wavelength at λ_{em} = 490 nm that will shift to λ_{em} = 420 nm when the surroundings become more ordered (Figure S5bi). The relationship between the maxima at those wavelengths is called the general polarization (GP) and gives an indication of level of order (or lower fluidity) of a lipid membrane (Figure S5bii). GUV^{Z} and GUV^{-} had similar negative GP, which were comparable to previously reported values.[11–13] However, a GP of ~0.4 was found for GUV^{S}, suggesting they had a less fluid membrane than GUV^{Z} and GUV^{-} in agreement with other reports.[14,15]

Following on, the different motors were encapsulated in the void of the GUVs during the assembly. Independent of the membrane composition or the motor size, all GUVs had encapsulated motors (Figure S5c). However, the number of motors inside the GUVs varied with the motor size, i.e., higher number of $^{0.5}M_M$ were encapsulated in the GUVs compared to $^{1}M_M$ and $^{4}M_M$. The motors seemed to have a preference to adhere to the inner leaflet of the GUVs rather than stochastically distribute in the void, since they accumulated more towards the edges compared to the center of the GUV as observable from epifluorescence microscopy images. The GUVs showed a general size between 200 – 600 µm independent of the lipid composition or the size of the encapsulated motors (Figure S5d). It should be noted that the encapsulation process was not very effective, and many motors were found in the surrounding solution. However, these motors (not encapsulated) allowed us to determine the average speed of the motors inside the GUVs, which was critical to identify those crossing the lipid membranes or not.

Table S2. Lipid mixture composition (in volume) to fabricate GUV.

GUV	**Volume (µL)**				
	Bio-PE (*25 mg mL^{-1}*)	*Rho-PE* (*1 mg mL^{-1}*)	*DOPC* (*25 mg mL^{-1}*)	*DPPC* (*25 mg mL^{-1}*)	*DOPS* (*25 mg mL^{-1}*)
GUV^{Z}	0.5	0.5	9.5	-	-
GUV^{-}	0.5	0.5	8.5	-	1.0
GUV^{50-}	0.5	0.5	4.5	-	5.0
GUV^{S}	0.5	0.5	-	9.5	-

All lipids were dissolved in chloroform.

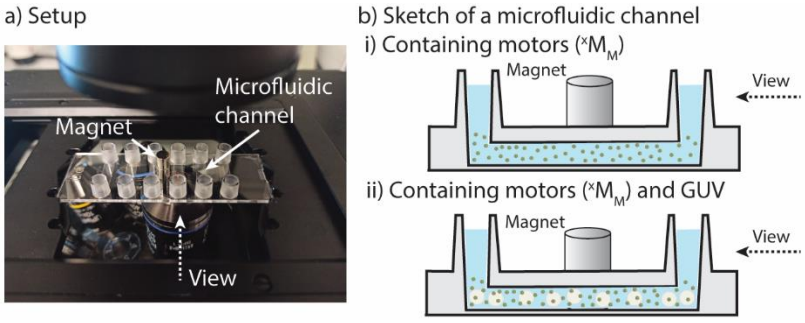

Figure S6. Experimental setup. a) Picture of the microfluidic channel mounted on an inverted bright-field microscope including the positioned magnet. b) Cartoon illustrating the solution containing only motors ($^{x}M_M$) (i) or motors and GUVs (ii). Dotted arrows indicate the view point.

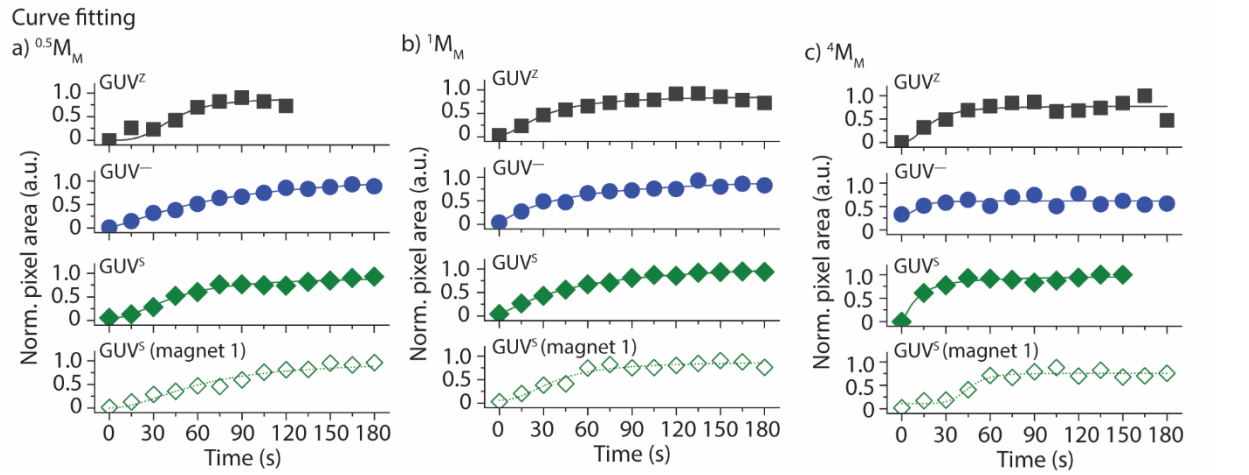

Figure S7. Filling rate curves of $^{0.5}M_M$, $^{1}M_M$ and $^{4}M_M$ crossing GUV. Open symbols indicate that magnet 1 was used instead of magnet 2. A logistic curve was fitted to the data.

Table S3. Characteristics of the $^{x}M_M$ crossing GUV membranes. The parameters were estimated from logistic curves (refer to Experimental Section). The parameters τ and p stand for the half-time the motors need to fill the GUVs and the filling rate, respectively.

	$^{0.5}M_M$		**$^{1}M_M$**		**$^{4}M_M$**	
	τ (s)	*p (s^{-1})*	*τ (s)*	*p (s^{-1})*	*τ (s)*	*p (s^{-1})*
GUV^{Z}	44	1.9	35	1.2	24	0.8
GUV^{-}	53	1.7	36	1.1	12*	0.1*
GUV^{50-}	8	2.3	-	-	-	-
GUV^{S}	46	1.6	36	1.5	10	1.2
GUV$^{S\,\#}$	67	1.9	41	1.4	51	1.3

* Due to the variability within the samples, these values could not be calculated reliably. # Magnet 1 was used instead of the magnet 2.

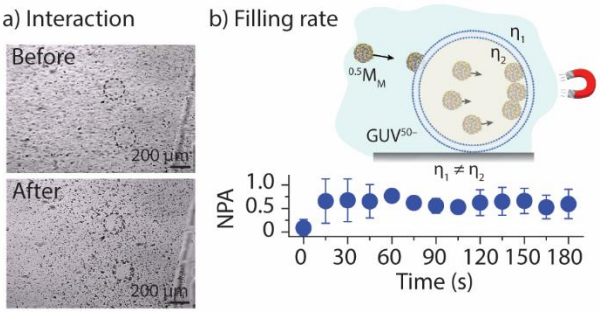

Figure S8. GUV containing 50% DOPS (GUV^{50-}). a) Representative bright-field microscopy images of the GUV containing $^{0.5}M_M$ and b) filling rate curves (NPA: normalized pixel area). Data are shown as mean ± standard deviation (n = 3).

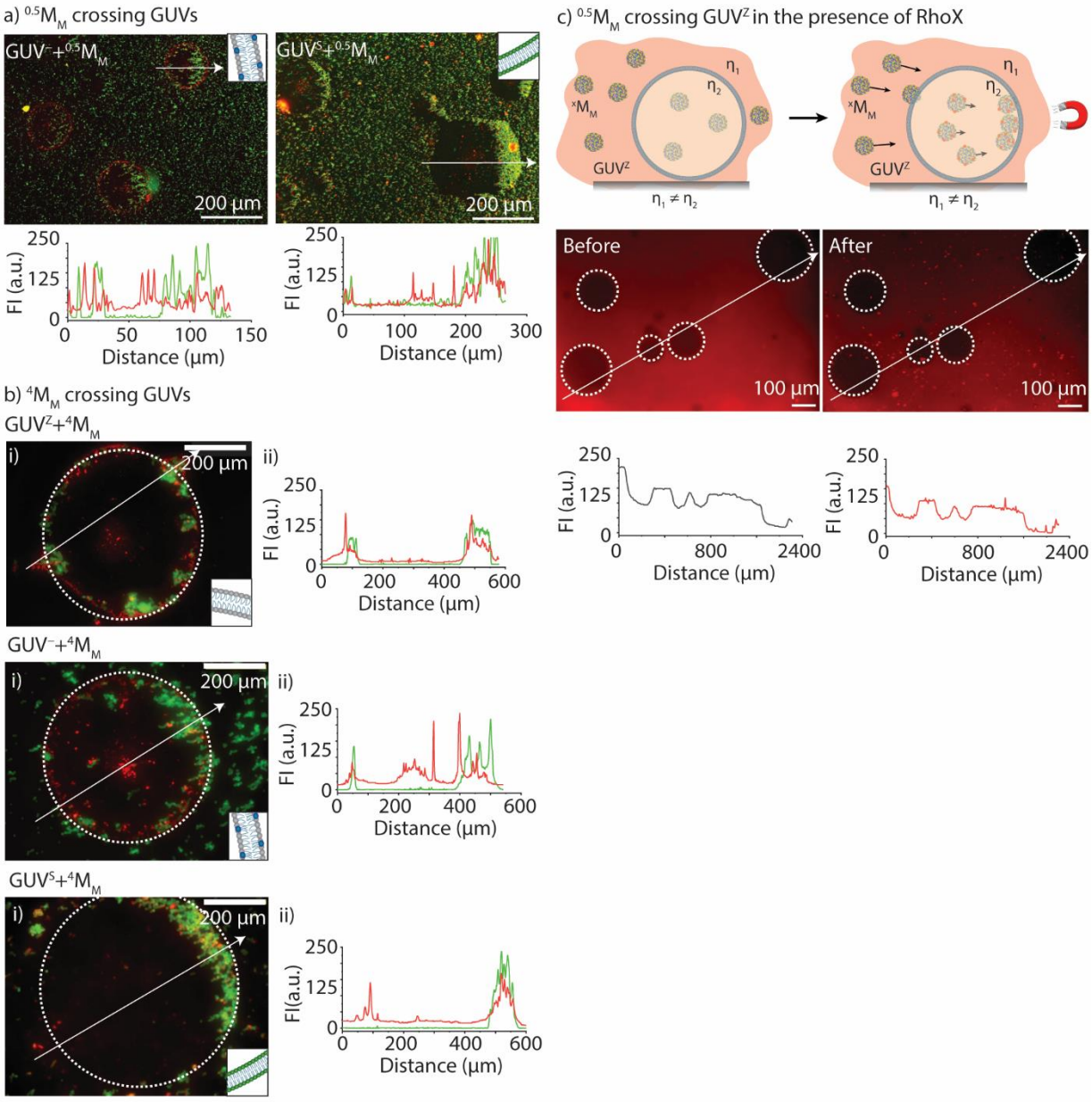

Figure S9. Representative epifluorescence microscopy images and the corresponding plot profiles of a) $^{0.5}M_M$ and b) ^4M_M crossing GUV^Z, GUV^- and GUV^S after applying magnet 2. (Green: PLL_{OG}, red: Rho-PE). c) $^{0.5}M_M$ crossing GUV^Z in the presence of RhoX in the presence of magnet 2. (Red: RhoX). The dotted circles are used to guide the eye indicating the GUVs. The white arrows indicate the profile path. (n = 2).

Table S4. Correlation coefficient analysis between $^{0.5}M_M$ or $^{4}M_M$ and GUVs.

	$^{0.5}\mathbf{M_M}$			$^{4}\mathbf{M_M}$		
	GUV^{Z}	*GUV*$^{-}$	*GUV*^{S}	*GUV*^{Z}	*GUV*$^{-}$	*GUV*^{S}
Pearson	0.360	0.640	0.650	0.640	0.180	0.780
Manders (red-to-green)	0.463	0.386	0.694	0.573	0.240	0.688
Manders (green-to-red)	0.659	0.705	0.725	0.984	0.375	0.953

Pearson's correlation coefficient is a parametric test that shows the linear relation between two sets of variables using a linear function. The numbers vary between (-1, 1), giving an estimate of how well the two variables relate (0 means no correlation whilst ±1 indicates total positive or negative correlation). Values of ~0.5 – 0.7 show a moderate correlation.

Manders' overlap coefficient also estimates the relationship between two sets of variables, with a range that varies between (0, 1). In particular, this coefficient provides the specific relation of the first data set in relation to the second, and *vice versa*, which is more suitable for colocalization purposes.

References

1 H. Zhou, C. C. Mayorga-Martinez, S. Pané, L. Zhang and M. Pumera, *Chem. Rev.*, 2021, **121**, 4999–5041.

2 P. De Dios Andres, M. A. Ramos-Docampo, X. Qian, M. Stingaciu and B. Städler, *Nanoscale*, 2021, **13**, 17900–17911.

3 P. de Dios Andres and B. Städler, *Small*, 2022, 2201251.

4 J. A. Vance and N. K. Devaraj, *J. Am. Chem. Soc.*, 2021, **143**, 8223–8231.

5 P. A. Beales, B. Ciani and A. J. Cleasby, *Phys. Chem. Chem. Phys.*, 2015, **17**, 15489–15507.

6 G. Tsuji, T. Sunami and N. Ichihashi, *J. Biosci. Bioeng.*, 2018, **126**, 540–545.

7 A. Moga, N. Yandrapalli, R. Dimova and T. Robinson, *ChemBioChem*, 2019, **20**, 2674–2682.

8 P. Walde, K. Cosentino, H. Engel and P. Stano, *ChemBioChem*, 2010, **11**, 848–865.

9 T. Parasassi, G. De Stasio, G. Ravagnan, R. M. Rusch and E. Gratton, *Biophys. J.*, 1991, **60**, 179–189.

10 A. G. Jay and J. A. Hamilton, *J. Fluoresc.*, 2017, **27**, 243–249.

11 M. M. Rahman, M. Ueda, T. Hirose and Y. Ito, *J. Am. Chem. Soc.*, 2018, **140**, 17956–17961.

12 N. Marušič, L. Otrin, Z. Zhao, R. B. Lira, F. L. Kyrilis, F. Hamdi, P. L. Kastritis, T. Vidakovic-Koch, I. Ivanov, K. Sundmacher and R. Dimova, *Proc. Natl. Acad. Sci. U. S. A.*, 2020, **117**, 15006–15017.

13 P. De Dios Andres, I. N. Westensee, E. Brodszkij, M. A. Ramos-Docampo, N. Gal and B. Städler, *Biomacromolecules*, 2021, **22**, 3860–3872.

14 K. Flandez, S. Bonardd and M. Soto-Arriaza, *Chem. Phys. Lipids*, 2020, **230**, 104927.

15 M. Paez-Perez, I. A. Russell, P. Cicuta and L. Di Michele, *Soft Matter*, 2022, **18**, 7035–7044.